THE JOURNAL OF PHYSICAL CHEMISTRY LETTERS
A JOURNAL OF THE AMERICAN CHEMICAL SOCIETY

pubs.acs.org/JPCL

Letter

Theoretical Design of Heavy-Atom Embedded ICz-Based Multi-resonance TADF Emitters with High Efficiency and Narrow Emission Width

Yaxin Wang and Zhigang Shuai*

Cite This: *J. Phys. Chem. Lett.* 2025, 16, 7752−7762

Read Online

ACCESS | Metrics & More | Article Recommendations | Supporting Information

ABSTRACT: Indolo[3,2,1-*jk*] carbazole (ICz)-based multiple resonance (MR) organic emitters bearing small full width at half-maximum (fwhm) values are of interest in organic light-emitting diodes. The challenge is to boost the intrinsic delayed fluorescence by enhancing the reverse intersystem crossing (RISC) process to avoid efficiency roll-off. Here, we propose the utilization of the nonmetallic heavy-atom effects to promote the RISC process while keeping the advantage of structural rigidity for narrowband emission. The emission spectrum and quantum efficiency were investigated by using quantum chemistry calculations coupled with our thermal vibration correlation function (TVCF) formalism. For heavy-atom embedded dICz-MR emitters, the synergistic effect of spin−vibronic coupling and spin−orbit coupling promotes the potential RISC channels ($T_1 \rightarrow T_2/T_3 \rightarrow S_1$), the effective k_{RISC}, up to 10^6 s^{-1}. Besides, heavy-atom embedded para-linked ICz-MR emitters have little effect on emission width due to the considerable structural rigidity and low-frequency dominated vibronic coupling.

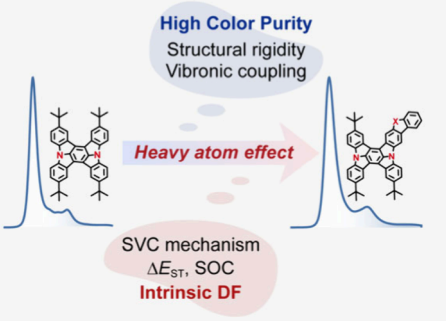

Multiple-resonance thermally activated delayed fluorescence (MR-TADF) organic light-emitting diodes (OLEDs) have emerged as promising candidates for next-generation ultrahigh-definition (UHD) displays due to their narrowband emission.[1−7] In 2016, Hatakeyama et al. reported the first MR-TADF emitter (DABNA-1) that utilizes antiphase resonance effects between boron and nitrogen atoms to achieve spatial separation of the highest occupied molecular orbital (HOMO) and lowest unoccupied molecular orbital (LUMO) at the atomic scale.[2] This unique electronic configuration facilitates short-range charge transfer (SRCT) while maintaining a rigid boron−nitrogen (B−N) framework, which has been shown to effectively minimize the energy gap (ΔE_{ST}) between the lowest singlet (S_1) and triplet (T_1) excited states.[8−12] Meanwhile, the combination of low-frequency vibronic coupling and structural rigidity results in a narrowband emission with full width at half-maximum (fwhm) < 30 nm, accompanied by a small Stokes shift.[13] Lately, plenty of analogues of B−N polycyclic aromatic hydrocarbons, such as B−O,[14−16] B−S,[17−19] N-carbonyl (N−C=O) frameworks,[20−22] have been intensively explored, but the commercial application of these boron-based emitters is still limited to a certain extent: (1) Commission Internationale de l'Éclairage (CIE) color coordinates do not satisfy the BT 2020 color standard despite their high EQE; (2) the relatively slow reverse intersystem crossing (RISC) rate constant (10^3−10^4 s^{-1}) may induce significant efficiency roll-off, substantially limiting operational device lifetimes. Recently, Yang's group developed Se-containing BN-MR emitters to increase the RISC rate constant,[23,24] while the embedded heavy atoms lead to a low color purity. Therefore, developing MR emitters with both high color purity and high emitting efficiency remains a challenge for UHD displays.[7,25]

Recently, a novel nitrogen-embedded MR framework for OLED application has been developed by fusing two or more indolo[3,2,1-*jk*] carbazole (ICz) units,[26−39] which provides a promising strategy to address the limitations in color purity. In 2020, Lee et al. first reported a pure violet emitter (mICz) by fusing two meta-positioned ICz units; the MR effect can be induced by the contrary electronegativities of carbon (C) and N atoms, resulting in the atomic HOMO−LUMO separation and narrowband emission, which exhibit exceptionally high color purity (fwhm = 14 at 393 nm center wavelength).[26] In addition, subsequent developments of para-positioned ICz-MR emitters[27,28] exhibited deep-blue emission (pICz: fwhm = 18 at 441 nm center wavelength; DICz: fwhm = 10 at 446 nm center wavelength), by taking advantage of the synergetic effect of para-positioned N atoms to reduce the energy gap. Among the three classical frameworks, only the pICz emitter exhibited

Received: April 22, 2025
Revised: July 15, 2025
Accepted: July 18, 2025

https://doi.org/10.1021/acs.jpclett.5c01218
J. Phys. Chem. Lett. 2025, 16, 7752−7762

Scheme 1. (a) Chemical Structures of the Reported Representative ICz-Based MR Frameworks, (b) Previous Work on Improving k_{RISC}, and (c) the Molecular Design Concept of Heavy-Atom Embedded ICz-MR Emitters in This Work

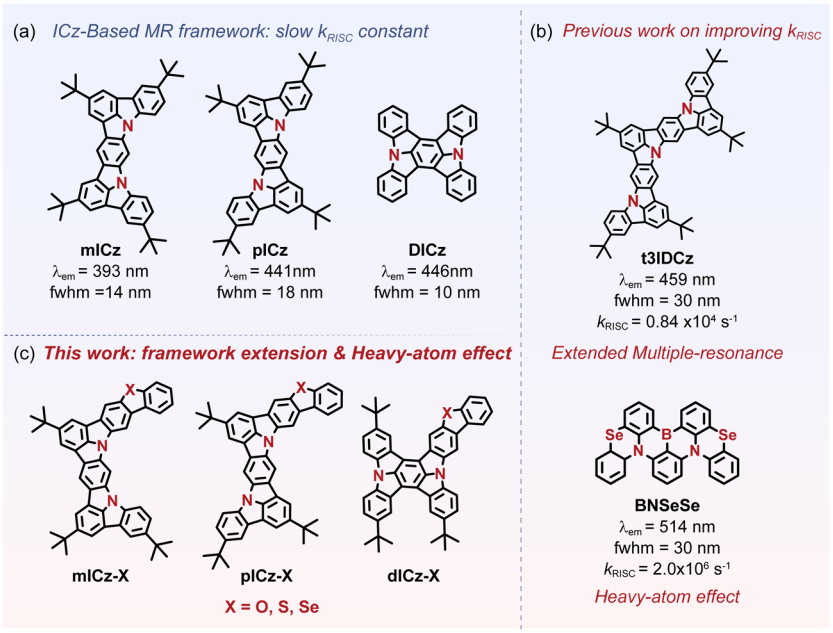

delayed fluorescence behavior, which Lee and co-workers attributed to a second-order spin-vibronic coupling (SVC)-assisted RISC process.[40] This mechanism relies critically on the S_1-T_1 energy gap being close to the T_1-T_2 energy gap; a significant deviation between these energy differences renders the SVC mechanism ineffective. Although numerous ICz-MR emitters with high color purity have been reported, their commercial viability is hindered by a low RISC rate constant.[35,37] To address this, Lee's group explored the extension of the pICz framework via meta- or para-positioned linkages and observed that para-linkages can enhance the MR effect, thereby increasing the RISC rate constant via the SVC effect.[33] Furthermore, our previous work also confirmed that para-linked extension is an effective strategy for achieving intrinsic delayed fluorescence.[41] However, despite the improvements in the RISC rate constant afforded by framework extensions, the rates remain relatively slow, underscoring the need for developing innovative approaches to further enhance RISC rate constants.

Herein, inspired by experimental findings that the heavy-atom effect can improve the photophysical properties of BN-MR emitters,[19,23,24,42] we propose a novel strategy that combines framework expansion with the heavy-atom effect to enhance RISC rate constants for ICz-MR systems. In this work, nine heavy-atom embedded ICz-MR emitters were systematically designed by combining a carbazole unit with meta- (mICz) or para-positioned ICz frameworks (pICz and dICz), in which heavy atoms (O, S, Se) were strategically embedded in the para position of the nitrogen atom to replace the carbon atom in the five-membered ring (Scheme 1). Compared to the meta-positioned ICz framework, the presence of heavy atoms has minimal impact on the structural rigidity and vibronic coupling of the para-linked system, resulting in a relatively narrow emission spectrum. Furthermore, the major contribution of heavy-atom effects to the RISC rate primarily depends on the alignment of energy level positions (induced SVC effects) rather than significantly enhancing spin−orbit coupling (SOC) effects. Triplet excitons can be harvested via activated $T_1 \rightarrow T_2/T_3 \rightarrow S_1$ channels and exhibit intrinsic delayed fluorescence characteristics. Our work establishes theoretical insights to enhance the RISC rate constants of ICz-based MR emitters and elucidates the critical role of heavy-atom effects on emitting efficiency and color purity. These findings may provide a valuable foundation for guiding experimental molecular design strategies.

Optical Spectra. To accurately characterize the luminescence properties of the ICz-MR emitters, we initially calculated their vertical excitation energy using 12 widely adopted hybrid and long-range-corrected density functionals, comparing the results with experimental data. Among these functionals, B3LYP exhibited the closest agreement with experimental values, with a minimal deviation of less than 0.05 eV (Table S1 and Figure S1). Consequently, we employed density functional theory (DFT) and time-dependent DFT (TD-DFT) methods at the B3LYP/6-311G(d,p) level to optimize the geometries of both the ground (S_0) and first excited (S_1) states using the Gaussian 16 software package.[49] All structures were confirmed to be free of imaginary frequencies, ensuring their stability. To further validate the computational benchmark for predicting luminescence properties, geometric displacements, structural deformations, and Duschinsky rotation effects between the S_0 and S_1 states were analyzed using the time-dependent thermal vibration correlation function (TVCF) method, as implemented in the MOMAP software.[43−48] By comparing the theoretical predictions of the full width at half-maximum (fwhm) of the emission bandwidth, as well as absorption (λ_{abs}) and emission (λ_{emi}) center wavelengths, with experimental results (Table S2), we observed excellent agreement in both the bandwidth and luminescence positions (error less than 10 nm). Therefore, from the perspectives of computational efficiency and accuracy, the TVCF method based on the B3LYP/6-311G (d,p) level demonstrates significant potential for predicting vibrationally resolved spectra in ICz-MR emitters. These results underscore the reliability of the TVCF method at the B3LYP level for accurately simulating

https://doi.org/10.1021/acs.jpclett.5c01218
J. Phys. Chem. Lett. 2025, 16, 7752−7762

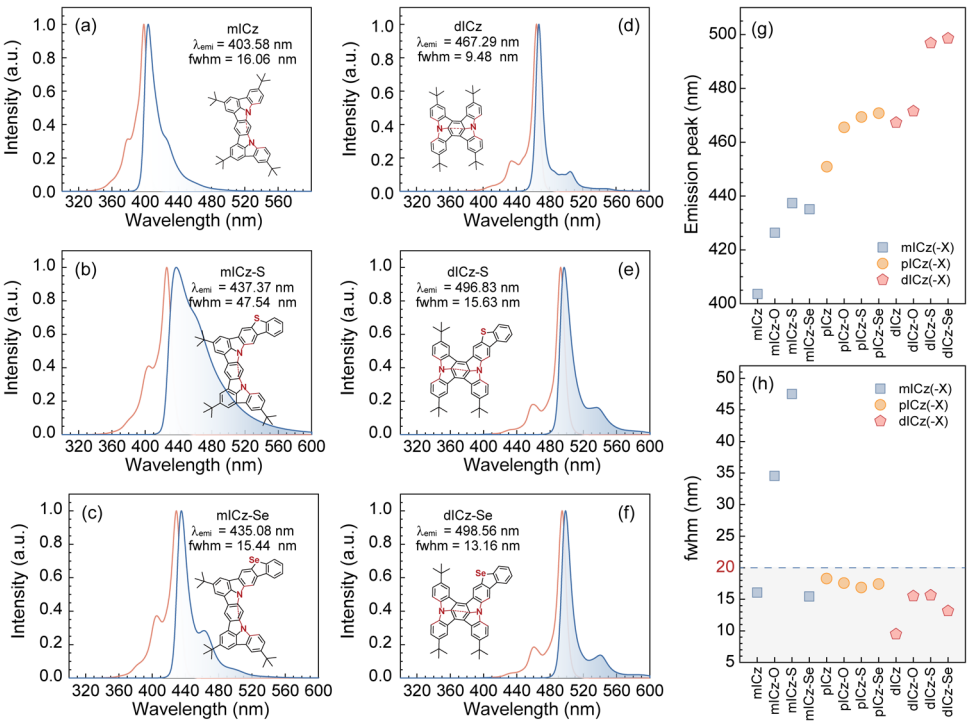

Figure 1. Absorption (red solid lines) and emission (blue filled bands) spectra of (a) mICz, (b) mICz-S, (c) mICz-Se, (d) dICz, (e) dICz-S, and (f) dICz-Se emitters. The calculated (g) fwhm and (h) emission peak positions of all ICz-MR emitters.

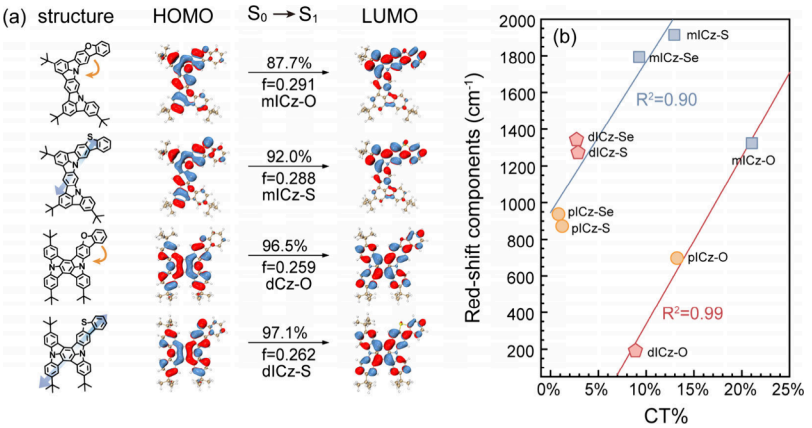

Figure 2. (a) HOMO/LUMO distribution of selected ICz-based MR emitters. (b) Correlation of calculated redshift components and CT% of S_1 state for heavy-atom embedded ICz-based MR emitters.

the luminescence properties of the investigated ICz-MR system.

The TVCF-calculated vibronic spectra of all investigated ICz-MR emitters are illustrated in Figure 1a–f and Figure S2, along with their corresponding λ_{emi} positions and emission fwhm values. Results show that (1) all heavy-atom embedded ICz-MR emitters exhibit emission redshifts relative to their corresponding ICz parent framework counterparts, with the magnitude of the redshift increasing with the atomic number of the heavy atoms (O > S > Se; Figure 1g). (2) The influence of the heavy-atom effect on color purity appears to depend on the parent framework connection mode; emitters show varying degrees of color purity, with para-linked compounds demonstrating fwhm values less than 20 nm (Figure 1h). In the following section, we will elucidate the mechanism underlying the heavy-atom effect on the redshift of emission spectra and color purity.

Redshift. In general, the emission spectral properties of emitters are fundamentally tied to the characteristics of their excited states, which can be qualitatively explored through computational analyses of frontier orbitals (FOs) and hole–electron distributions. Notably, as noted by Oliver et al., TD-DFT may fail to predict excited-state energies and the nature of S_1 for most functionals, except for CAM-B3LYP, with the SCS-CC2 method being recommended as a more reliable alternative.[50] In this work, we opted for the TD-DFT method to achieve a balance between computational efficiency and accuracy given the substantial computational demands of SCS-CC2. Additionally, considering the well-documented precision of the B3LYP functional in reproducing molecular spectra, we began by comparing the excitation state results derived from the B3LYP and CAM-B3LYP calculations. As shown in Table S3, we found that the natural transition orbitals (NTO), hole–electron distribution, and charge density difference (CDD)

https://doi.org/10.1021/acs.jpclett.5c01218
J. Phys. Chem. Lett. 2025, 16, 7752–7762

Table 1. Calculated Emission Bandwidth (fwhm), RMSD, $\Gamma_{S1\rightarrow S0}$, Frequency, and HR Factor of the Dominant Mode in Vibronic Coupling

				Dominant vibrational mode		
	fwhm (cm^{-1})	RMSD (Å)	$\Gamma_{S1\rightarrow S0}$ (cm^{-1})	Frequency (cm^{-1})	HR factor	Counts (HR > 0.1)
mICz	971.91	0.035	972.91	104.24	0.44	4
mICz-O	1813.25	0.039	1154.43	71.99	0.47	4
mICz-S	2338.88	0.038	912.93	70.44	0.42	5
mICz-Se	809.45	0.036	853.18	69.35	0.34	4
pICz	889.85	0.045	966.58	69.16	0.58	4
pICz-O	805.16	0.043	931.02	62.53	0.65	4
pICz-S	761.21	0.042	851.85	61.28	0.62	4
pICz-Se	781.42	0.042	826.29	60.09	0.64	3
dICz	433.32	0.040	412.20	58.89	0.55	1
dICz-O	690.13	0.034	425.34	57.76	0.38	1
dICz-S	627.67	0.037	410.10	56.86	0.36	2
dICz-Se	526.79	0.037	415.96	56.33	0.36	3

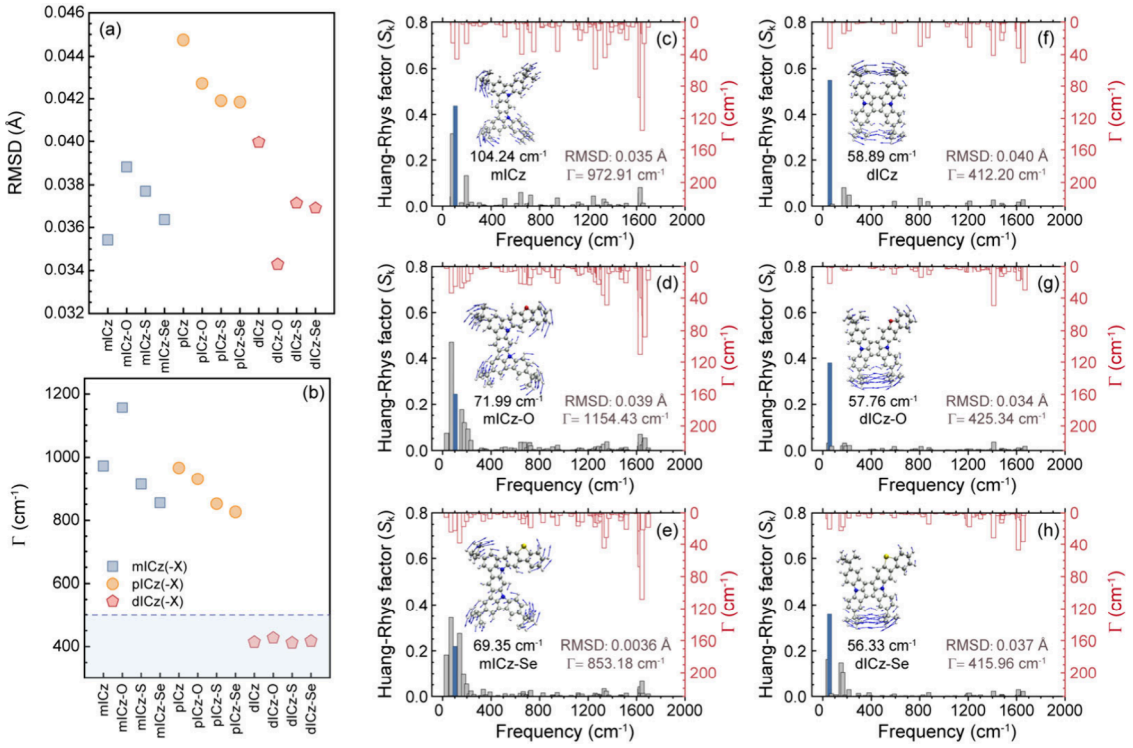

Figure 3. (a) RMSD analysis and (b) reorganization energy of all ICz-MR emitters; calculated HR factors of each vibrational mode in $S_1 \rightarrow S_0$ transition of (c–e) mICz-X and (f–h) dICz-X emitters. Vibration vectors of modes with large Huang–Rhys factors or reorganization energy contribution are shown as insets.

descriptions provided by B3LYP were highly consistent with CAM-B3LYP calculations for ICz-MR emitters. Consequently, we utilized the B3LYP/6-311G(d,p) level to calculate the vertical transitions of the low-lying singlet (S_1 to S_3) and triplet (T_1 to T_3) excited states. As summarized in Table S4, the $S_0 \rightarrow S_1$ transitions in all ICz-MR emitters are predominantly governed by the HOMO and LUMO, for which we further visualized the spatial distribution of frontier orbitals (FOs) using the Multiwfn[51] and VMD 1.9.3[52] programs.

The results demonstrate that while the heavy-atom effect has a minimal impact on the HOMO level (showing slight increases correlated with heavy-atom electronegativity), it significantly lowers the LUMO level of the investigated ICz-MR emitters. This reduction leads to a decrease in the HOMO–LUMO gap, which is macroscopically manifested as a redshift in the emission spectrum (Figure S3). In parent frameworks (mICz, pICz, dICz), the FO distribution of the S_1 state exhibits SRCT characteristics with MR effects, displaying localized atomic and near-uniform electron density distributions, consistent with previous reports.[26−29] In contrast, heavy-atom embedded ICz-MR emitters display two distinct HOMO/LUMO distribution patterns, primarily governed by the electronegativity of the heavy atoms. As illustrated in Figure 2a and Figure S3, the HOMO/LUMO distribution of the three O-embedded emitters (mICz-O, pICz-O, and dICz-O) is nonuniform across the framework. Specifically, the LUMO distribution shifts toward the heavy-atom positions, while the heavy-atom effect contributes minimally to the HOMO distribution, which suggests that the underlying O-embedded emitters may exhibit long-range charge transfer

https://doi.org/10.1021/acs.jpclett.5c01218
J. Phys. Chem. Lett. 2025, 16, 7752−7762

(LRCT) characteristics. Conversely, S- and Se-embedded ICz-MR emitters exhibit more uniform HOMO/LUMO distributions throughout the framework, indicating enhanced MR effects through heavy-atom electronegativity modulation that accentuates the peripheral unit charge distribution.

Moreover, meta-linked emitters generally exhibit more pronounced CT components than their para-linked counterparts (Figure 2b), and the CT component decreases with increasing electronegativity for the same linkage mode, consistent with our earlier conclusions. Notably, two distinct linear relationships (R^2 = 0.90/0.99) were established between the red-shift component and the CT% of heavy-atom embedded ICz-MR emitters. Specifically, O-embedded emitters display CT% higher than that of S/Se-embedded emitters, where redshift originates from LRCT mechanisms. In contrast, S/Se-embedded emitters exhibit reduced CT% but enhanced MR effects as the primary redshift drivers. These findings establish a clear structure−property relationship between heavy-atom-induced electronic modifications and excited-state characteristics in ICz-MR emitters.

Color Purity. As mentioned above, the influence of heavy-atom effect on color purity appears to depend on the parent framework connection mode. Among them, all ICz-MR emitters exhibit primary emission peaks accompanied by distinct vibrational shoulder features, with notable variations in shoulder intensity. In meta-linked configurations, the heavy-atom effect (O/S) significantly enhances the vibronic shoulder intensity, resulting in broader emission profiles. Conversely, the heavy-atom effect (Se) diminishes the shoulder intensity, leading to a narrower emission bandwidth. Notably, the heavy-atom effect has minimal influence on the shoulder strength of para-linked configurations. These para-linked emitters consistently maintain exceptional color purity (fwhm < 20 nm), regardless of the heteroatom incorporated.

The color purity of OLED emitters is fundamentally determined by two intrinsic material properties: structural rigidity and vibronic coupling characteristics.[53] To elucidate the structure−property relationships and the mechanistic role of the heavy-atom effect on the color purity of different molecular frameworks, we systematically analyzed their electronic structures and vibrational properties of all investigated emitters. The geometric structures of the investigated heavy-atom embedded ICz-MR emitters were optimized using DFT/TD-DFT approaches for the S_0 and S_1 states at the B3LYP/6-311G(d,p) level (Table S5). Our calculations reveal high structural rigidity in all ICz-MR emitters, as evidenced by a fully coplanar configuration of atomic positions and minimal structural relaxation between the S_0 and S_1 states. Consequently, quantifying structural relaxation using specific bond lengths or dihedral angles proved to be challenging. To address this, we calculated the root mean square displacement (RMSD) analysis and reorganization energy (Γ) calculations between the S_0 and S_1 states to quantitatively evaluate structural relaxation in heavy-atom embedded ICz-MR emitters. A direct comparison of the optimized S_1/S_0 geometries and their corresponding RMSD values is provided in Figure S4 and Table 1.

As shown in Figure 3a, the investigated ICz-MR emitters exhibit minimal structural distortion ($RMSD_{S1/S0}$ < 0.05 Å) during the $S_1 \rightarrow S_0$ transition, indicating a rigid ICz-based framework. Interestingly, the heavy-atom effect increases RMSD values in meta-linkage compared to the parent framework, whereas para-linked derivatives exhibit significantly reduced RMSD values. This suggests that the heavy-atom effect is configuration-dependent: (1) enhancing geometric relaxation in meta-linked systems and (2) suppressing structural relaxation in para-linked systems. Furthermore, the change trend of the $\Gamma_{S1\rightarrow S0}$ value is similar to that of RMSD, with the dICz system showing a minimal $\Gamma_{S1\rightarrow S0}$ value (Figure 3b). Besides, within the same parent framework, the $\Gamma_{S1\rightarrow S0}$ value of emitters will decrease with the increase in the atomic radius of heavy atoms, indicating that larger atomic radii effectively inhibit structural relaxation. However, both $\Gamma_{S1\rightarrow S0}$ and RMSD values are reduced for mICz-S ($\Gamma_{S1\rightarrow S0}$ = 912.93 cm^{-1}, RMSD = 0.038 Å) emitters compared to the mICz-O emitter ($\Gamma_{S1\rightarrow S0}$ = 1154.43 cm^{-1}, RMSD = 0.039 Å), while the mICz-S emitter exhibits a broader emission spectrum (fwhm = 2338.88 cm^{-1}), indicating that additional factors may influence color purity.

Therefore, we calculated the vibronic coupling between electronic (S_1) and vibrational (ν = 0, 1, 2, ...) transitions to elucidate the mechanism of the influence of heavy-atom effects on color purity, which is described by the Huang−Rhys (HR) factor of vibrational modes involved in $S_1 \rightarrow S_0$ transition.[53−55] As illustrated in Figure 3c−h and Figure S5, all investigated ICz-MR emitters exhibited a small HR factor (S_k < 0.7) for their dominant vibronic coupling modes, with the dominant vibrational coupling modes located in the low-frequency region (<100 cm^{-1}), indicating weak coupling between electronic and vibrational transitions. Besides, para-linked emitters display both reduced dominant vibrational frequencies and fewer vibrational modes compared with those of meta-linkage (Table 1), correlating with improved color purity in electroluminescence applications. Additionally, the vibrational mode of the ICz-MR emitter shifts to lower frequencies upon embedding heavy atoms, thereby promoting narrowband emission. Notably, heavy-atom effects display distinct configuration-dependent manifestations: (1) For meta-linked systems, O- and S- atoms embedded emitters induce additional vibrational modes in both the low-frequency region (∼100 cm^{-1}) and high-frequency region (>1000 cm^{-1}), resulting in a broader spectrum compared to the mICz parent framework. Among these, mICz-S exhibits the highest number of vibrational modes. Despite its suppressed structural relaxation, it still demonstrates a broader emission spectrum compared with the mICz-O emitter. In contrast, the mICz-Se emitter shows a significant reduction in the HR factor, indicating that increasing the atomic radius of heavy atoms can attenuate vibrational coupling, suppress shoulder peak intensity, and achieve a narrower emission spectrum. (2) The HR factor strength of the pICz parent framework increases due to the heavy-atom effect, while their counts decrease when the atomic radius increases, which helps to improve the color purity. In addition, although the heavy-atom effect introduces additional vibration modes for the dICz-X emitter, it also greatly reduces the strength of the HR factor, and combined with minimized structural relaxation, this configuration achieves the highest color purity.

Based on the above discussion, the superior color purity observed in heavy-atom embedded ICz-MR emitters primarily originates from two synergistic mechanisms: significant structural rigidity (minimizing S_1/S_0 structural relaxation) and low-frequency dominated weak vibronic coupling. Among them, the embedded heavy-atom demonstrates a negligible impact on structural relaxation within para-linked emitters while effectively inducing weak vibronic coupling primarily in

https://doi.org/10.1021/acs.jpclett.5c01218
J. Phys. Chem. Lett. 2025, 16, 7752−7762

Table 2. Summary of Calculated ΔE_{ST}*, SOC Matrix Element, Fluorescence Quantum Yield (Φ_f), and Rate Constants of Investigated ICz-based MR Emitters

		mICz	mICz-O	mICz-S	mICz -Se	pICz	pICz-O
ΔE_{ST}* (eV)	S_1-T_1	0.67	0.64	0.60	0.59	0.50	0.44
	S_1-T_2/S_1-T_3	0.43/<0.01	0.50/0.41	0.46/0.38	0.43/0.36	0.07/0.03	0.36/−0.09
SOC (cm^{-1})	T_1-S_1	0.34	0.44	0.47	0.58	0.49	0.47
	T_2-S_1/ T_3-S_1	0.09/0.07	0.37/0.07	0.31/0.05	0.35/0.15	0.20/0.01	0.09/0.03
k_r (s^{-1})		8.42×10^7	2.88×10^7	4.13×10^7	5.05×10^7	2.53×10^7	1.62×10^7
k_{IC} (s^{-1})		3.36×10^2	2.49×10^4	3.29×10^6	5.61×10^2	-4.28×10^1	2.73×10^3
k_{ISC} (s^{-1})	$S_1 \rightarrow T_1$	5.82×10^6	1.61×10^7	2.84×10^7	1.74×10^7	6.07×10^6	2.73×10^6
	$S_1 \rightarrow T_2$	5.42×10^6	4.59×10^3	7.02×10^6	5.32×10^6	3.24×10^7	4.50×10^7
	$S_1 \rightarrow T_3$	1.91×10^6	3.28×10^6	5.20×10^6	1.95×10^6	3.28×10^5	4.25×10^3
[a]Φ_{PF}		86.49%	59.76%	48.47%	67.18%	39.47%	25.29%
η_r		0.00%	0.00%	0.02%	0.00%	100.00%	12.31%
k_{RISC} (s^{-1})	$T_1 \rightarrow S_1$	3.03×10^{-5}	2.91×10^{-4}	2.48×10^{-3}	2.61×10^{-3}	2.07×10^{-2}	1.04×10^{-1}
	$T_2 \rightarrow S_1$	3.34×10^{-1}	2.09×10^{-5}	1.28×10^{-1}	2.78×10^{-1}	2.09×10^6	3.70×10^1
	$T_3 \rightarrow S_1$	1.82×10^6	4.92×10^{-1}	2.02×10 °	1.74×10 °	8.75×10^4	1.23×10^5
		pICz -S	**pICz -Se**	**dICz**	**dICz-O**	**dICz -S**	**dICz -Se**
ΔE_{ST}* (eV)	S_1-T_1	0.40	0.42	0.61	0.60	0.56	0.56
	S_1-T_2/S_1-T_3	0.15/−0.06	0.35/0.16	0.14/0.1	0.07/0.05	0.04/−0.02	0.05/<0.01
SOC (cm^{-1})	T_1-S_1	0.47	0.44	0.55	0.45	0.39	0.46
	T_2-S_1	0.17/0.15	0.21/0.09	<0.01/<0.01	0.09/0.02	0.15/0.01	0.15/0.05
k_r (s^{-1})		2.36×10^7	2.69×10^7	6.94×10^7	8.52×10^7	6.89×10^7	6.15×10^7
k_{IC} (s^{-1})		1.79×10^3	1.81×10^3	4.27×10^2	1.45×10^2	3.89×10^2	4.15×10^3
k_{ISC} (s^{-1})	$S_1 \rightarrow T_1$	4.18×10^6	2.18×10^6	1.41×10^1	1.30×10^6	4.03×10^5	1.49×10^6
	$S_1 \rightarrow T_2$	7.36×10^7	3.75×10^7	1.08×10^8	1.32×10^8	3.19×10^8	3.89×10^8
	$S_1 \rightarrow T_3$	6.30×10^3	3.06×10^6	1.68×10^3	9.56×10^4	1.77×10^5	3.06×10^5
[a]Φ_{PF}		23.26%	38.64%	39.14%	38.96%	94.47%	13.60%
η_r		94.36%	13.65%	99.96%	100.00%	100.00%	99.98%
k_{RISC} (s^{-1})	$T_1 \rightarrow S_1$	8.86×10^{-1}	2.19×10^{-1}	9.42×10^{-10}	1.10×10^{-4}	1.43×10^{-4}	5.37×10^{-4}
	$T_2 \rightarrow S_1$	1.99×10^5	5.96×10^1	5.77×10^5	7.85×10^6	6.34×10^7	5.12×10^7
	$T_3 \rightarrow S_1$	5.58×10^4	5.30×10^3	1.52×10^2	1.68×10^4	4.39×10^5	2.89×10^5

[a]Calculated as $\Phi_f = k_r/(k_r + k_{IC} + k_{ISC}^{S1\rightarrow T1} + k_{ISC}^{S1\rightarrow T2} + k_{ISC}^{S1\rightarrow T3})$.

low-frequency modes, thereby preserving the intrinsic color purity of the ICz framework. Furthermore, although the embedded heavy atom may introduce additional vibrational modes (accompanied by relatively large RMSD and recombination energies), resulting in spectral broadening, the strategic selection of heavy atoms with larger atomic radii mitigates structural relaxation and weakens vibronic coupling. This ultimately leads to a narrowing of the emission spectrum and enhanced color purity.

Emitting Efficiency. As a key factor in the performance of OLED devices, the external quantum efficiency (EQE) of corresponding organic emitters is defined as the ratio between the number of emitted photons to injected carriers. Typically, the η_{EQE} of OLED devices can be expressed as the product of several contributing terms:

$$\eta_{EQE} = \gamma \times \eta_r \times \Phi_F \times \eta_{out} \quad (1)$$

where the carrier balance factor (γ) and output coupling factor (η_{out}) depend on device design and fabrication, respectively. The exciton utilization efficiency (η_r) and fluorescent quantum yield (Φ_F) are regarded as intrinsic properties of the emitters closely tied to their excited-state behavior.[9,56,57] Specifically, Φ_F includes a contribution from the S_1 state directly generated by injected carriers (Φ_{PF}, prompt fluorescence) and converted from the T_1 state (Φ_{DF}, delayed fluorescence), which is determined by competition between radiative and nonradiative decay of the emitting S_1 state.[58−60] Besides, η_r reflects the harvesting efficiency of triplet excitons via reverse intersystem crossing (RISC) processes,[41,57,61] requiring the RISC rate (k_{RISC}) constant to surpass competing triplet relaxation mechanisms.

As shown in Table S4, the vertical energies calculated by TD-DFT indicate that the T_1 and T_2 states lie lower in energy than the S_1 state, leading to a positive vertical energy gap. In some cases, some T_3 states are slightly above or below the S_1 state. Consequently, for the ICz-MR system, contributions of the T_1−T_3 states to RISC cannot be overlooked. Therefore, given the multiple RISC pathways available in the investigated emitters, we employ the effective RISC rate (k_{RISC}^{eff}) constant as a metric to quantify the enhancement induced by the heavy-atom effect.

$$k_{RISC}^{eff} = k_{RISC}^{T_1\rightarrow S_2} + k_{RISC}^{T_2\rightarrow S_1}\exp\left(\frac{E_{T_1} - E_{T_2}}{k_B T}\right) + k_{RISC}^{T_3\rightarrow S_1}\exp\left(\frac{E_{T_1} - E_{T_3}}{k_B T}\right) \quad (2)$$

To quantitatively assess the emitting efficiency of investigated ICz-MR emitters, the excited-state decay rate constants were calculated by using the TVCF method. Notably, within the TVCF framework, all electronic structure calculations strictly employ stable configurations (in the absence of imaginary frequencies) for both initial and final states. In addition, accurate calculations of electron−vibration coupling (EVC) require consistent handling of the initial and final states

https://doi.org/10.1021/acs.jpclett.5c01218
J. Phys. Chem. Lett. 2025, 16, 7752−7762

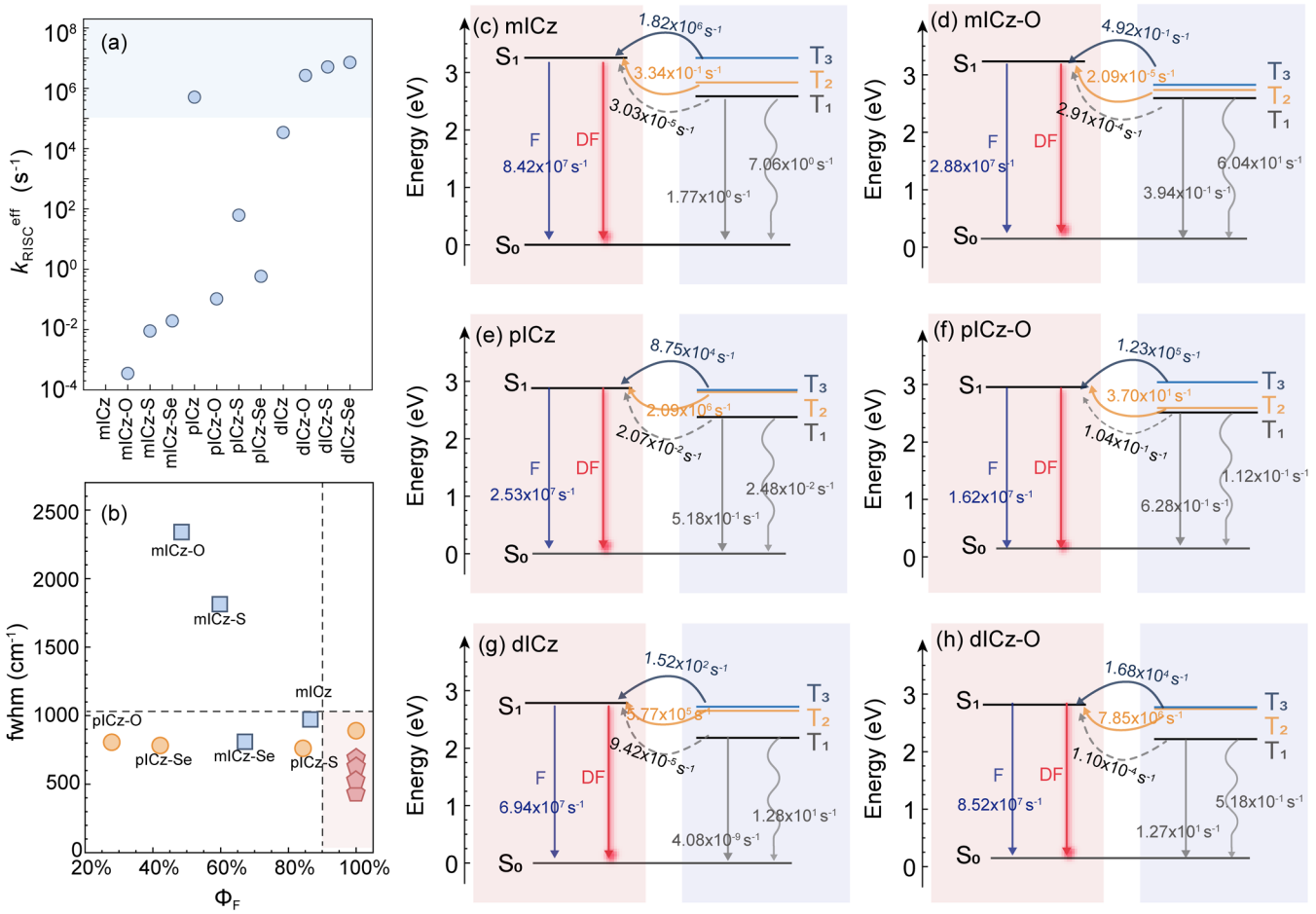

Figure 4. (a) The calculated effective RISC rate constants, and (b) the relationship between the fwhm and Φ_F of investigated ICz-MR emitters. Emission mechanism of (c) mICz, (d) mICz-O, (e) pICz, (f) pICz-O, (g) dICz, and (h) dICz-O emitters.

at the same level of computation; otherwise, vibration analysis would be meaningless. The detailed methodology and relevant equations for rate constant calculations are provided in the Supporting Information and follow the procedures established in our previous work.[43−48]

Given the established accuracy of the B3LYP/6-311g(d,p) level in reproducing vibrationally resolved optical spectra, as demonstrated in our preliminary calculations, we employed this level of theory for geometry optimizations of all relevant triplet excited-state structures. All of the corresponding decay rate constants involved in the transition process are shown in Table 2. First, we compared the error between a series of rate constants calculated using the TVCF method and the experimental values; the calculated radiative decay rate (k_r) constant for pICz emitter is 2.53×10^7 s^{-1}, which is reasonably close to the experimentally reported value of 6.25×10^7 s^{-1}.[62] However, it is important to note that this method is primarily qualitative and better suited for determining whether delayed fluorescence is present than for precise quantitative analysis. For example, the calculated RISC rate constant for the mICz emitter is notably low, indicating a lack of delayed fluorescence; while the experimental RISC rate constant for the pICz emitter is 10^3 s^{-1}, the calculated value is 10^5 s^{-1}. Therefore, we prefer to compare the trend of the heavy-atom effect on the molecular RISC rate to elucidate its impact on the intrinsic delayed fluorescence mechanism rather than quantitative prediction of absolute rate constants. By focusing on systematic variations in heavy-atom effect induced RISC efficiency, we aim to create structure−property relationships and try to uncover physical insights into the mechanism of heavy-atom effects on ICz-MR emitters.

Notably, significant efforts have been made in improving the accuracy of RISC rate predictions, such as utilizing the SCS-CC2 or TDA-B2PLYP method.[19,50] These approaches have yielded results closer to experimental values, with the predicted rate constant within the same order of magnitude. However, for ICz-MR emitters, the intrinsic rigidity of the molecular plane and the presence of intersection points between excited states introduce unique challenges. Structural optimizations of highly excited states for these molecules often converge to the same minimum energy point or result in imaginary frequencies. Moreover, the application of advanced methods like the SCS-CC2 or TDA-B2PLYP method is both computationally expensive and less operable for ICz-MR emitters. Accordingly, our results aim to highlight the dominant mechanisms and general trends in how the heavy-atom effect influences RISC processes in ICz-MR emitters rather than to provide highly precise quantitative predictions. Future studies may focus on incorporating hybrid computational strategies or exploring alternative theoretical frameworks to further refine the accuracy of RISC rate estimations.

As summarized in Table 2, the heavy-atom embedded ICz-MR emitters exhibit minimal impact on the k_r constant (~10^7 s^{-1}) compared to the ICz framework. However, the

https://doi.org/10.1021/acs.jpclett.5c01218
J. Phys. Chem. Lett. 2025, 16, 7752−7762

quantitative contribution of the corresponding singlet state (Φ_{PF}) for the ICz-based MR emitters varies significantly, ranging from ∼20% to nearly 100% (e.g., dICz-S), primarily due to the competition between the k_r constant and the intersystem crossing rate (k_{ISC}) (Figure S6a). However, the results demonstrate that the triplet relaxation channels are strongly influenced by the linkage manner of the parent framework. Specifically, the triplet excitons of the dICz system are effectively converted into singlet states via the RISC process owing to the high k_{RISC} ratio, resulting in enhanced exciton utilization (Figure S6b). In contrast, for the meta-linked mICz-X systems and the O-/Se-incorporated pICz emitters, the k_{RISC} constants do not exhibit a definitive advantage over the k_{nrt} constants. This suggests that these molecules may lack delayed fluorescence properties.

As illustrated in Figure 4a, the effective RISC rate constant significantly increases with the increase in the atomic number of embedded heavy atoms. Notably, while the heavy-atom effect enhances the RISC rate constant of meta-linked emitters by up to 3 orders of magnitude, the overall RISC rate remains sluggish. Furthermore, these emitters exhibit a broader fwhm and lower luminescence quantum yield (Φ_{PF}), as depicted in Figure 4b, constraining their applicability in UHD display technologies. Conversely, the heavy-atom effect substantially boosts the effective RISC rate constant of para-linked dICz-X emitters (10^6 s^{-1}), enabling these emitters to exhibit intrinsic delayed fluorescence characteristics. Additionally, the para-linked dICz system demonstrates both narrowband emission and high Φ_{PF}, suggesting that this framework may play an important role in next-generation UHD displays. However, the heavy-atom effect appears to diminish or even eliminate the delayed fluorescence characteristics of the para-linked pICz system.

To further elucidate this mechanism, we calculated the excited-state energy levels and spin−orbit coupling of the emitters. Notably, vertical excitation energies (ΔE_{ST}) derived from TD-DFT are often unreliable for MR-type emitters, with these methods frequently yielding notable discrepancies between theoretical predictions and experimental measurements (Table S6). Such limitations necessitate the implementation of high-level computational approaches (specifically double hybrid functionals or multireference methods) for accurate energy determination. However, the investigated ICz-MR systems present inherent computational challenges arising from potential energy surface (PES) crossings. To address this challenges, we estimated the adiabatic excitation energies (ΔE_{ST}*) by optimizing the geometries of the S_1, T_1, T_2, and T_3 states, i.e., the global minimum on the PES of the corresponding states (Table S6 and Figure S7). In addition, we calculated SOC matrix elements by using the linear response approach implemented in the PySOC program[63] as shown in Table 2 and Figure S8. For heavy-atom embedded meta-linked emitters, the $SOC_{T1\text{-}S1}$ matrix elements show an increasing trend with the atomic numbers of O, S, and Se. In contrast, the $SOC_{T1\text{-}S1}$ matrix elements of para-linked emitters display no substantial variation, particularly for the dICz-X emitter, where the $SOC_{T1\text{-}S1}$ matrix assembly is lower than that of the parent framework. Additionally, the $SOC_{T2\text{-}S1}$ and $SOC_{T3\text{-}S1}$ matrix elements are considerably smaller than those of $SOC_{T1\text{-}S1}$ for all investigated ICz-MR emitters, which may significantly impact the corresponding RISC rate constant.

To further understand the different trends in SOC matrix elements with the atomic numbers of O, S, and Se in the investigated ICz-MR emitters, we performed electron density calculations in the excited states of each molecule and generated charge density difference (CDD) data and visualizations (Table S7). Results show that the contribution of heavy atoms increases with atomic number; their overall contribution to CDD remains small (<15% for O, S, and Se). Consequently, the SOC matrix elements do not increase proportionally with the atomic number. We employed meta-linked mICz-X emitters to explain the origin of largely different $SOC^{T1\text{-}S1}$, $SOC^{T2\text{-}S1}$, and $SOC^{T3\text{-}S1}$ matrix elements. The result shows that the CDD of the S_1 state is more evenly distributed across the framework and the heavy atom, with the CDD at the heavy atom being negative (−1.73, −7.17, and −12.49% for O, S, and Se). In contrast, the CDD of the T_1 state is primarily localized at the head of the framework, significantly differing from the S_1 state distribution, and the CDD is positive (0.47, 0.14, and 0.25% for O, S, and Se, respectively). This large difference in orbital angular momentum between the S_1 and T_1 states results in a large SOC. However, the CDD distribution of the T_2 state shows less difference from the S_1 state (with the T_3 state showing the least difference), and the CDD at the heavy atom remains negative. This indicates a smaller angular momentum difference, leading to a smaller SOC value.

Besides, as shown in Table 2 and Figure S9, the heavy-atom effect significantly reduces the singlet (S_1) and triplet state (T_1, T_2, T_3) energy levels while enhancing the corresponding SOC matrix elements for meta-linked emitters compared with the parent framework. Despite these modifications, the RISC channels ($T_1 \rightarrow S_1$, $T_2 \rightarrow S_1$, and $T_3 \rightarrow S_1$) remain kinetically unfavorable due to the thermally inaccessible ΔE_{ST} (0.3−0.7 eV) for the mICz system (Figure 4c,d and Figure S10). Notably, the tert-butyl-modified pICz and dICz parent frameworks demonstrate nearly equivalent S_1−T_1 and T_1−T_2 energy gaps, thereby enabling the SVC mechanism ($T_1 \rightarrow T_2 \rightarrow S_1$) to establish a feasible RISC pathway for delayed fluorescence emission (Figure 4e,g). Intriguingly, although both pICz and dICz are para-linked frameworks, the heavy-atom effects exhibit a strikingly distinct modulation of molecular energy levels. Specifically, the heavy-atom effect significantly lowers the T_2 energy level, thereby disrupting the SVC mechanism for pICz-X system (Figure 4f). Concurrently, the implantation of O- and S-embedded derivatives elevates the T_3 energy level above S_1, coupled with an increased SOC matrix element, resulting in dramatically accelerated $k_{RISC}^{T3\rightarrow S1}$. However, based on the Boltzmann distribution under thermal equilibrium conditions, the effective RISC rate remains insufficient to enable efficient delayed fluorescence. In contrast, the heavy-atom effect in dICz derivatives induces energy-level compression between S_1-T_1 and T_1-T_2 states, which enables SVC-driven RISC ($T_1 \rightarrow T_2 \rightarrow S_1$) with minimal thermal activation barriers (Figure 4h and Figure S10). Here, our calculation proved the rationality of SVC mechanism for achieving efficient RISC: (1) for the investigated mICz, mICz-X, and pICz-X emitters of both T_1 and T_2 to S_1 state, structural modification is needed for opening the $T_2 \rightarrow S_1$ RISC channel by lifting the T_2 state energetically; (2) for pICz, dICz, and dICz-X emitters, the considerable $k_{RISC}^{T2\rightarrow S1}/k_{RISC}^{T3\rightarrow S1}$ is dominantly contributed by energetically matching S_1−T_1 and T_1−T_2/T_3 gaps, i.e., minimized ΔE_{ST} (S_1−T_2/T_3), which can be further optimized by structural modification on fused heavy-atom and tert-butyl units to achieve faster k_{RISC}^{eff} than other relaxation channels.

https://doi.org/10.1021/acs.jpclett.5c01218
J. Phys. Chem. Lett. 2025, 16, 7752−7762

To further verify that the heavy-atom effect and framework extension can synergistically enhance the RISC rate constant of the investigated ICz-MR emitters, we conducted comparative computational analyses on extended frameworks without heavy-atom incorporation, including mICz-C, pICz-C, and dICz-C (Figure S11). When evaluating these nonheavy-atom systems, framework extension alone produced only moderate increases in the RISC rate constant for both meta- and para-linked emitters. However, when heavy atoms are embedded, we observed significant rate constant amplifications, providing clear computational evidence for the synergistic interplay between framework extension and heavy-atom effects in ICz-MR emitters. Furthermore, we calculated the photophysical and luminescence properties of these emitters. Consistent with earlier findings, meta-linked mICz-C emitters exhibit low color purity with broad emission spectra (fwhm > 2000 cm^{-1}). In contrast, para-linked dICz-C emitters demonstrated narrower emission spectra and higher color purity. These results suggest that para-linked dICz frameworks are promising candidates for UHD display technology, offering both high color purity and efficient exciton utilization.

In conclusion, we conducted a comprehensive theoretical investigation into the photophysical and emissive properties of heavy-atom embedded ICz-MR emitters. The calculated vibrationally resolved spectra and excited state decay rate constants revealed that the heavy-atom effect on the color purity and emitting efficiency of the emitter is strongly modulated by the framework connectivity. In particular, the minimized S_1/S_0 structural relaxation and the low-frequency dominated vibronic coupling significantly contribute to their superior color purity for the para-linked dICz system. Furthermore, the enhancement of RISC rate constants is primarily attributed to the fine-tuned energy-level alignment and increased SOC matrix elements, which facilitate potential RISC channels ($T_1 \rightarrow T_2/T_3 \rightarrow S_1$), thereby enabling intrinsic delayed fluorescence. Our work provides valuable insights into the origin of color purity and emission efficiency in heavy-atom embedded ICz-MR systems. We anticipate that these findings will provide theoretical insights into the molecular design and development of ICz-MR emitters, advancing their application in high-performance OLED devices, particularly for next-generation UHD displays.

■ ASSOCIATED CONTENT

Supporting Information

The Supporting Information is available free of charge at https://pubs.acs.org/doi/10.1021/acs.jpclett.5c01218.

Methodology; performance of different TD-DFT functionals; TVCF calculated optical spectrum; excited-state properties under different functionals; vertical excited states; HOMO/LUMO distribution and energy levels; optimized structure of ground and excited states; RMSD; reorganization energy and Huang−Rhys factor; singlet and triplet relaxation channels; calculated ΔE_{ST}*, ΔE_{ST}, and SOC matrix element; charge density difference (CDD) analysis; calculated adiabatic energies and decay rates constants; comparison of structure and properties (PDF)

■ AUTHOR INFORMATION

Corresponding Author

Zhigang Shuai − *School of Science and Engineering, The Chinese University of Hong Kong, Shenzhen 518172, People's Republic of China; MOE Key Laboratory of Organic OptoElectronics and Molecular Engineering, Department of Chemistry, Tsinghua University, 100084 Beijing, People's Republic of China;* orcid.org/0000-0003-3867-2331; Email: shuaizhigang@cuhk.edu.cn

Author

Yaxin Wang − *School of Science and Engineering, The Chinese University of Hong Kong, Shenzhen 518172, People's Republic of China*

Complete contact information is available at: https://pubs.acs.org/10.1021/acs.jpclett.5c01218

Notes

The authors declare no competing financial interest.

■ ACKNOWLEDGMENTS

This work is supported by the National Natural Science Foundation of China (Grant Nos. T2350009 and 22433007), the Guangdong Provincial Natural Science Foundation (grant nos. 2024A1515011185), and the Shenzhen City Peacock Team Project (grant no. KQTD20240729102028011). Y.W. is supported by the China Postdoctoral Science Foundation (no. 2025M771052).

■ REFERENCES

(1) Hong, G.; Gan, X.; Leonhardt, C.; Zhang, Z.; Seibert, J.; Busch, J. M.; Bräse, S. A Brief History of OLEDs—Emitter Development and Industry Milestones. *Adv. Mater.* **2021**, *33* (9), 2005630.

(2) Hatakeyama, T.; Shiren, K.; Nakajima, K.; Nomura, S.; Nakatsuka, S.; Kinoshita, K.; Ni, J.; Ono, Y.; Ikuta, T. Ultrapure Blue Thermally Activated Delayed Fluorescence Molecules: Efficient HOMO−LUMO Separation by the Multiple Resonance Effect. *Adv. Mater.* **2016**, *28* (14), 2777−2781.

(3) Kondo, Y.; Yoshiura, K.; Kitera, S.; Nishi, H.; Oda, S.; Gotoh, H.; Sasada, Y.; Yanai, M.; Hatakeyama, T. Narrowband Deep-Blue Organic Light-Emitting Diode Featuring an Organoboron-Based Emitter. *Nat. Photonics* **2019**, *13* (10), 678−682.

(4) Naveen, K. R.; Yang, H. I.; Kwon, J. H. Double Boron-Embedded Multiresonant Thermally Activated Delayed Fluorescent Materials for Organic Light-Emitting Diodes. *Commun. Chem.* **2022**, *5* (1), 1−14.

(5) Matsui, K.; Oda, S.; Yoshiura, K.; Nakajima, K.; Yasuda, N.; Hatakeyama, T. One-Shot Multiple Borylation toward BN-Doped Nanographenes. *J. Am. Chem. Soc.* **2018**, *140* (4), 1195−1198.

(6) Li, X.; Shi, Y.-Z.; Wang, K.; Zhang, M.; Zheng, C.-J.; Sun, D.-M.; Dai, G.-L.; Fan, X.-C.; Wang, D.-Q.; Liu, W.; Li, Y.-Q.; Yu, J.; Ou, X.-M.; Adachi, C.; Zhang, X.-H. Thermally Activated Delayed Fluorescence Carbonyl Derivatives for Organic Light-Emitting Diodes with Extremely Narrow Full Width at Half-Maximum. *ACS Appl. Mater. Interfaces* **2019**, *11* (14), 13472−13480.

(7) Dos Santos, J. M.; Hall, D.; Basumatary, B.; Bryden, M.; Chen, D.; Choudhary, P.; Comerford, T.; Crovini, E.; Danos, A.; De, J.; Diesing, S.; Fatahi, M.; Griffin, M.; Gupta, A. K.; Hafeez, H.; Hämmerling, L.; Hanover, E.; Haug, J.; Heil, T.; Karthik, D.; Kumar, S.; Lee, O.; Li, H.; Lucas, F.; Mackenzie, C. F. R.; Mariko, A.; Matulaitis, T.; Millward, F.; Olivier, Y.; Qi, Q.; Samuel, I. D. W.; Sharma, N.; Si, C.; Spierling, L.; Sudhakar, P.; Sun, D.; Tankelevičiūtė, E.; Duarte Tonet, M.; Wang, J.; Wang, T.; Wu, S.; Xu, Y.; Zhang, L.; Zysman-Colman, E. The Golden Age of Thermally Activated Delayed Fluorescence Materials: Design and Exploitation. *Chem. Rev.* **2024**, *124* (24), 13736−14110.

(8) Zhang, Y.; Zhang, D.; Wei, J.; Hong, X.; Lu, Y.; Hu, D.; Li, G.; Liu, Z.; Chen, Y.; Duan, L. Achieving Pure Green Electroluminescence with CIEy of 0.69 and EQE of 28.2% from an Aza-Fused Multi-Resonance Emitter. *Angew. Chem., Int. Ed.* **2020**, *59* (40), 17499−17503.
(9) Cai, X.; Pu, Y.; Li, C.; Wang, Z.; Wang, Y. Multi-Resonance Building-Block-Based Electroluminescent Material: Lengthening Emission Maximum and Shortening Delayed Fluorescence Lifetime. *Angew. Chem., Int. Ed.* **2023**, *62* (27), No. e202304104.
(10) Wang, Q.; Xu, Y.; Huang, T.; Qu, Y.; Xue, J.; Liang, B.; Wang, Y. Precise Regulation of Emission Maxima and Construction of Highly Efficient Electroluminescent Materials with High Color Purity. *Angew. Chem., Int. Ed.* **2023**, *62* (19), No. e202301930.
(11) Valverde, D.; Ser, C. T.; Ricci, G.; Jorner, K.; Pollice, R.; Aspuru-Guzik, A.; Olivier, Y. Computational Investigations of the Detailed Mechanism of Reverse Intersystem Crossing in Inverted Singlet−Triplet Gap Molecules. *ACS Appl. Mater. Interfaces* **2024**, *16* (49), 66991−67001.
(12) Pu, Y.-J.; Valverde, D.; Sancho-García, J. C.; Olivier, Y. Computational Design of Multiple Resonance-Type BN Molecules for Inverted Singlet and Triplet Excited States. *J. Phys. Chem. A* **2023**, *127* (48), 10189−10196.
(13) Uoyama, H.; Goushi, K.; Shizu, K.; Nomura, H.; Adachi, C. Highly Efficient Organic Light-Emitting Diodes from Delayed Fluorescence. *Nature* **2012**, *492* (7428), 234−238.
(14) Hirai, H.; Nakajima, K.; Nakatsuka, S.; Shiren, K.; Ni, J.; Nomura, S.; Ikuta, T.; Hatakeyama, T. One-Step Borylation of 1,3-Diaryloxybenzenes Towards Efficient Materials for Organic Light-Emitting Diodes. *Angew. Chem., Int. Ed.* **2015**, *54* (46), 13581−13585.
(15) Ahn, D. H.; Kim, S. W.; Lee, H.; Ko, I. J.; Karthik, D.; Lee, J. Y.; Kwon, J. H. Highly Efficient Blue Thermally Activated Delayed Fluorescence Emitters Based on Symmetrical and Rigid Oxygen-Bridged Boron Acceptors. *Nat. Photonics* **2019**, *13* (8), 540−546.
(16) Ahn, D. H.; Maeng, J. H.; Lee, H.; Yoo, H.; Lampande, R.; Lee, J. Y.; Kwon, J. H. Rigid Oxygen-Bridged Boron-Based Blue Thermally Activated Delayed Fluorescence Emitter for Organic Light-Emitting Diode: Approach towards Satisfying High Efficiency and Long Lifetime Together. *Adv. Opt. Mater.* **2020**, *8* (11), 2000102.
(17) Chen, F.; Zhao, L.; Wang, X.; Yang, Q.; Li, W.; Tian, H.; Shao, S.; Wang, L.; Jing, X.; Wang, F. Novel Boron- and Sulfur-Doped Polycyclic Aromatic Hydrocarbon as Multiple Resonance Emitter for Ultrapure Blue Thermally Activated Delayed Fluorescence Polymers. *Sci. China Chem.* **2021**, *64* (4), 547−551.
(18) Chang, Y.; Wu, Y.; Wang, X.; Li, W.; Yang, Q.; Wang, S.; Shao, S.; Wang, L. Boron, Sulfur-Doped Polycyclic Aromatic Hydrocarbon Emitters with Multiple-Resonance-Dominated Lowest Excited States for Efficient Narrowband Deep-Blue Emission. *Chem. Eng. J.* **2023**, *451*, 138545.
(19) Shizu, K.; Kaji, H. Quantitative Prediction of Rate Constants and Its Application to Organic Emitters. *Nat. Commun.* **2024**, *15* (1), 4723.
(20) Yuan, Y.; Tang, X.; Du, X.-Y.; Hu, Y.; Yu, Y.-J.; Jiang, Z.-Q.; Liao, L.-S.; Lee, S.-T. The Design of Fused Amine/Carbonyl System for Efficient Thermally Activated Delayed Fluorescence: Novel Multiple Resonance Core and Electron Acceptor. *Adv. Opt. Mater.* **2019**, *7* (7), 1801536.
(21) Min, H.; Park, I. S.; Yasuda, T. Cis-Quinacridone-Based Delayed Fluorescence Emitters: Seemingly Old but Renewed Functional Luminogens. *Angew. Chem., Int. Ed.* **2021**, *60* (14), 7643−7648.
(22) Wu, S.; Kumar Gupta, A.; Yoshida, K.; Gong, J.; Hall, D.; Cordes, D. B.; Slawin, A. M. Z.; Samuel, I. D. W.; Zysman-Colman, E. Highly Efficient Green and Red Narrowband Emissive Organic Light-Emitting Diodes Employing Multi-Resonant Thermally Activated Delayed Fluorescence Emitters. *Angew. Chem., Int. Ed.* **2022**, *61* (52), No. e202213697.
(23) Hua, T.; Zhan, L.; Li, N.; Huang, Z.; Cao, X.; Xiao, Z.; Gong, S.; Zhou, C.; Zhong, C.; Yang, C. Heavy-Atom Effect Promotes Multi-Resonance Thermally Activated Delayed Fluorescence. *Chem. Eng. J.* **2021**, *426*, 131169.
(24) Hu, Y. X.; Miao, J.; Hua, T.; Huang, Z.; Qi, Y.; Zou, Y.; Qiu, Y.; Xia, H.; Liu, H.; Cao, X.; Yang, C. Efficient Selenium-Integrated TADF OLEDs with Reduced Roll-Off. *Nat. Photonics* **2022**, *16* (11), 803−810.
(25) Chan, C.-Y.; Tanaka, M.; Lee, Y.-T.; Wong, Y.-W.; Nakanotani, H.; Hatakeyama, T.; Adachi, C. Stable Pure-Blue Hyperfluorescence Organic Light-Emitting Diodes with High-Efficiency and Narrow Emission. *Nat. Photonics* **2021**, *15* (3), 203−207.
(26) Lee, H. L.; Chung, W. J.; Lee, J. Y. Narrowband and Pure Violet Organic Emitter with a Full Width at Half Maximum of 14 Nm and y Color Coordinate of Below 0.02. *Small* **2020**, *16* (14), 1907569.
(27) Wei, J.; Zhang, C.; Zhang, D.; Zhang, Y.; Liu, Z.; Li, Z.; Yu, G.; Duan, L. Indolo[3,2,1-Jk]Carbazole Embedded Multiple-Resonance Fluorophors for Narrowband Deep-Blue Electroluminescence with EQE 34.7% and CIEy 0.085. *Angew. Chem., Int. Ed.* **2021**, *60* (22), 12269−12273.
(28) Liu, T.; Cheng, C.; Lou, W.; Deng, C.; Liu, J.; Wang, D.; Tsuboi, T.; Zhang, Q. Ultrapure Blue Organic Light-Emitting Diodes Exhibiting 13 Nm Full Width at Half-Maximum. *J. Mater. Chem. C* **2022**, *10* (20), 7799−7802.
(29) Zeng, X.; Wang, X.; Zhang, Y.; Meng, G.; Wei, J.; Liu, Z.; Jia, X.; Li, G.; Duan, L.; Zhang, D. Nitrogen-Embedded Multi-Resonance Heteroaromatics with Prolonged Homogeneous Hexatomic Rings. *Angew. Chem., Int. Ed.* **2022**, *61* (14), No. e202117181.
(30) Luo, M.; Li, W.; Lyu, L.; Li, D.; Du, S.; Zhao, M.; Wang, Z.; Zhang, J.; Li, Y.; Ge, Z. Frontier Molecular Orbitals Regulation Enables Efficient and Ultraviolet to Deep-Blue Narrowband Emission. *Adv. Opt. Mater.* **2023**, *11* (2), 2202176.
(31) Zhang, Y.; Li, G.; Wang, L.; Huang, T.; Wei, J.; Meng, G.; Wang, X.; Zeng, X.; Zhang, D.; Duan, L. Fusion of Multi-Resonance Fragment with Conventional Polycyclic Aromatic Hydrocarbon for Nearly BT.2020 Green Emission. *Angew. Chem., Int. Ed.* **2022**, *61* (24), No. e202202380.
(32) Wang, X.; Duan, L.; Zhang, D. Indolocarbazole-Based Multiple-Resonance Molecules: An Emerging Class of Full-Color, Narrowband Emitters for Organic Light-Emitting Diodes. *Chem. − Eur. J.* **2023**, *29* (37), No. e202300701.
(33) Lee, H. L.; Jeon, S. O.; Kim, I.; Kim, S. C.; Lim, J.; Kim, J.; Park, S.; Chwae, J.; Son, W.-J.; Choi, H.; Lee, J. Y. Multiple-Resonance Extension and Spin-Vibronic-Coupling-Based Narrowband Blue Organic Fluorescence Emitters with Over 30% Quantum Efficiency. *Adv. Mater.* **2022**, *34* (33), 2202464.
(34) Zeng, X.; Wang, L.; Dai, H.; Huang, T.; Du, M.; Wang, D.; Zhang, D.; Duan, L. Orbital Symmetry Engineering in Fused Polycyclic Heteroaromatics toward Extremely Narrowband Green Emissions with an FWHM of 13 Nm. *Adv. Mater.* **2023**, *35* (22), 2211316.
(35) Luo, M.; Li, W.; Du, S.; Zhang, J.; Wang, Z.; Zhang, X.; Li, Y.; Ge, Z. Purely Nitrogen-Based Multi-Resonance Deep-Blue Emitter with an Ultralow y Color Coordinate of < 0.03 via Rationally Intramolecular Charge Transfer. *Adv. Opt. Mater.* **2023**, *11*, 2300491.
(36) Wang, Z.; Yan, Z.; Chen, Q.; Song, X.; Liang, J.; Ye, K.; Zhang, Z.; Bi, H.; Wang, Y. Toward Narrowband and Efficient Blue Fluophosphors by Locking the Stretching Vibration of Indolocarbazole Skeletons. *ACS Appl. Mater. Interfaces* **2023**, *15* (11), 14605−14613.
(37) Kang, J.; Lee, H. L.; Jeon, S. O.; Bae, H. J.; Kim, S. C.; Han, S.; Lee, J. Y. Spin-Flip-Restricted Multiple-Resonance Emitters for Extended Device Lifetime in Indolocarbazole-Based Blue Organic Light-Emitting Diodes. *Adv. Sci.* **2024**, *11* (40), 2405604.
(38) Wang, Y.; Yang, W.; Zhang, H.; Li, N.; Gong, S.; Gao, X.; Yang, C. Pyrazine-Fused Polycyclic Aromatic Hydrocarbons towards Efficient Multiple-Resonance Narrowband Deep-Blue Emission. *Sci. China Chem.* **2025**, *68* (3), 1018−1025.
(39) Keruckiene, R.; Vaitusionak, A. A.; Hulnik, M. I.; Berezianko, I. A.; Gudeika, D.; Macionis, S.; Mahmoudi, M.; Volyniuk, D.; Valverde, D.; Olivier, Y.; Woon, K. L.; Kostjuk, S. V.; Reineke, S.; Grazulevicius,

https://doi.org/10.1021/acs.jpclett.5c01218
J. Phys. Chem. Lett. 2025, 16, 7752−7762

J. V.; Sini, G. Is a Small Singlet−Triplet Energy Gap a Guarantee of TADF Performance in MR-TADF Compounds? Impact of the Triplet Manifold Energy Splitting. *J. Mater. Chem. C* **2024**, *12* (10), 3450−3464.
(40) Patil, V. V.; Lee, H. L.; Kim, I.; Lee, K. H.; Chung, W. J.; Kim, J.; Park, S.; Choi, H.; Son, W.-J.; Jeon, S. O.; Lee, J. Y. Purely Spin-Vibronic Coupling Assisted Triplet to Singlet Up-Conversion for Real Deep Blue Organic Light-Emitting Diodes with Over 20% Efficiency and y Color Coordinate of 0.05. *Adv. Sci.* **2021**, *8* (20), 2101137.
(41) Wang, Y.; Tian, Y.; Gao, Y.; Guo, Z.; Xue, Z.; Han, Y.; Yang, W.; Ma, X. Resolving the Photophysics of Nitrogen-Embedded Multiple Resonance Emitters: Origin of Color Purity and Emitting Efficiency. *J. Phys. Chem. Lett.* **2023**, *14* (43), 9665−9676.
(42) Shizu, K.; Ren, Y.; Kaji, H. Promoting Reverse Intersystem Crossing in Thermally Activated Delayed Fluorescence via the Heavy-Atom Effect. *J. Phys. Chem. A* **2023**, *127* (2), 439−449.
(43) Niu, Y.; Li, W.; Peng, Q.; Geng, H.; Yi, Y.; Wang, L.; Nan, G.; Wang, D.; Shuai, Z. MOlecular MAterials Property Prediction Package (MOMAP) 1.0: A Software Package for Predicting the Luminescent Properties and Mobility of Organic Functional Materials. *Mol. Phys.* **2018**, *116* (7−8), 1078−1090.
(44) Shuai, Z. Thermal Vibration Correlation Function Formalism for Molecular Excited State Decay Rates. *Chin. J. Chem.* **2020**, *38* (11), 1223−1232.
(45) Peng, Q.; Yi, Y.; Shuai, Z.; Shao, J. Toward Quantitative Prediction of Molecular Fluorescence Quantum Efficiency: Role of Duschinsky Rotation. *J. Am. Chem. Soc.* **2007**, *129* (30), 9333−9339.
(46) Niu, Y.; Peng, Q.; Shuai, Z. Promoting-Mode Free Formalism for Excited State Radiationless Decay Process with Duschinsky Rotation Effect. *Sci. China Ser. B Chem.* **2008**, *51* (12), 1153−1158.
(47) Peng, Q.; Yi, Y.; Shuai, Z.; Shao, J. Excited State Radiationless Decay Process with Duschinsky Rotation Effect: Formalism and Implementation. *J. Chem. Phys.* **2007**, *126* (11), 114302.
(48) Niu, Y.; Peng, Q.; Deng, C.; Gao, X.; Shuai, Z. Theory of Excited State Decays and Optical Spectra: Application to Polyatomic Molecules. *J. Phys. Chem. A* **2010**, *114* (30), 7817−7831.
(49) Frisch, M. J.; Trucks, G. W.; Schlegel, H. B.; Scuseria, G. E.; Robb, M. A.; Cheeseman, J. R.; Scalmani, G.; Barone, V.; Petersson, G. A.; Nakatsuji, H.; et al. *Gaussian 16*, Rev. A.03; 2016.
(50) Hall, D.; Sancho-García, J. C.; Pershin, A.; Ricci, G.; Beljonne, D.; Zysman-Colman, E.; Olivier, Y. Modeling of Multiresonant Thermally Activated Delayed Fluorescence Emitters−Properly Accounting for Electron Correlation Is Key. *J. Chem. Theory Comput.* **2022**, *18* (8), 4903−4918.
(51) Lu, T.; Chen, F. Multiwfn: A Multifunctional Wavefunction Analyzer. *J. Comput. Chem.* **2012**, *33* (5), 580−592.
(52) Humphrey, W.; Dalke, A.; Schulten, K. VMD: Visual Molecular Dynamics. *J. Mol. Graph.* **1996**, *14* (1), 33−38.
(53) Qiu, X.; Tian, G.; Lin, C.; Pan, Y.; Ye, X.; Wang, B.; Ma, D.; Hu, D.; Luo, Y.; Ma, Y. Narrowband Emission from Organic Fluorescent Emitters with Dominant Low-Frequency Vibronic Coupling. *Adv. Opt. Mater.* **2021**, *9* (4), 2001845.
(54) Peng, Q.; Fan, D.; Duan, R.; Yi, Y.; Niu, Y.; Wang, D.; Shuai, Z. Theoretical Study of Conversion and Decay Processes of Excited Triplet and Singlet States in a Thermally Activated Delayed Fluorescence Molecule. *J. Phys. Chem. C* **2017**, *121* (25), 13448−13456.
(55) Wang, L.; Ou, Q.; Peng, Q.; Shuai, Z. Theoretical Characterizations of TADF Materials: Roles of ΔG and the Singlet−Triplet Excited States Interconversion. *J. Phys. Chem. A* **2021**, *125* (7), 1468−1475.
(56) Cai, X.; Xu, Y.; Pan, Y.; Li, L.; Pu, Y.; Zhuang, X.; Li, C.; Wang, Y. Solution-Processable Pure-Red Multiple Resonance-Induced Thermally Activated Delayed Fluorescence Emitter for Organic Light-Emitting Diode with External Quantum Efficiency over 20%. *Angew. Chem., Int. Ed.* **2023**, *62* (7), No. e202216473.
(57) Chen, H.; Fan, T.; Zhao, G.; Zhang, D.; Li, G.; Jiang, W.; Duan, L.; Zhang, Y. A Simple Molecular Design Strategy for Pure-Red Multiple Resonance Emitters. *Angew. Chem., Int. Ed.* **2023**, *62* (20), No. e202300934.
(58) Li, Z.-W.; Peng, L.-Y.; Song, X.-F.; Chen, W.-K.; Gao, Y.-J.; Fang, W.-H.; Cui, G. Room-Temperature Phosphorescence and Thermally Activated Delayed Fluorescence in the Pd Complex: Mechanism and Dual Upconversion Channels. *J. Phys. Chem. Lett.* **2021**, *12* (25), 5944−5950.
(59) Notsuka, N.; Nakanotani, H.; Noda, H.; Goushi, K.; Adachi, C. Observation of Nonradiative Deactivation Behavior from Singlet and Triplet States of Thermally Activated Delayed Fluorescence Emitters in Solution. *J. Phys. Chem. Lett.* **2020**, *11* (2), 562−566.
(60) Zhang, K.; Yang, F.; Zhang, Y.; Ma, Y.; Fan, J.; Fan, J.; Wang, C.-K.; Lin, L. Highly Efficient Near-Infrared Thermally Activated Delayed Fluorescence Molecules via Acceptor Tuning: Theoretical Molecular Design and Experimental Verification. *J. Phys. Chem. Lett.* **2021**, *12* (7), 1893−1903.
(61) Gao, Y.; Wang, Y.; Guo, Z.; Wan, Y.; Li, C.; Yang, B.; Yang, W.; Ma, X. Ultrafast Photophysics of Multiple-Resonance Ultrapure Blue Emitters. *J. Phys. Chem. B* **2022**, *126* (14), 2729−2739.
(62) Patil, V. V.; Lee, H. L.; Kim, I.; Lee, K. H.; Chung, W. J.; Kim, J.; Park, S.; Choi, H.; Son, W.-J.; Jeon, S. O.; Lee, J. Y. Purely Spin-Vibronic Coupling Assisted Triplet to Singlet Up-Conversion for Real Deep Blue Organic Light-Emitting Diodes with Over 20% Efficiency and y Color Coordinate of 0.05. *Adv. Sci.* **2021**, *8* (20), 2101137.
(63) Gao, X.; Bai, S.; Fazzi, D.; Niehaus, T.; Barbatti, M.; Thiel, W. Evaluation of Spin-Orbit Couplings with Linear-Response Time-Dependent Density Functional Methods. *J. Chem. Theory Comput.* **2017**, *13* (2), 515−524.

https://doi.org/10.1021/acs.jpclett.5c01218
J. Phys. Chem. Lett. 2025, 16, 7752−7762